Metallization of diamond

Zhe Shi[a,b,1], Ming Dao[a,1,2], Evgenii Tsymbalov[c], Alexander Shapeev[c], Ju Li[a,b,2], and Subra Suresh[a,d,2]

[a]Department of Materials Science and Engineering, Massachusetts Institute of Technology, Cambridge, MA 02139; [b]Department of Nuclear Science and Engineering, Massachusetts Institute of Technology, Cambridge, MA 02139; [c]Skolkovo Institute of Science and Technology, 121205 Moscow, Russia; and [d]Nanyang Technological University, 639798 Singapore, Republic of Singapore

This contribution is part of the special series of Inaugural Articles by members of the National Academy of Sciences elected in 2012.

Contributed by Subra Suresh, August 7, 2020 (sent for review July 8, 2020; reviewed by Javier Llorca and Nicola Marzari)

Experimental discovery of ultralarge elastic deformation in nanoscale diamond and machine learning of its electronic and phonon structures have created opportunities to address new scientific questions. Can diamond, with an ultrawide bandgap of 5.6 eV, be completely metallized, solely under mechanical strain without phonon instability, so that its electronic bandgap fully vanishes? Through first-principles calculations, finite-element simulations validated by experiments, and neural network learning, we show here that metallization/demetallization as well as indirect-to-direct bandgap transitions can be achieved reversibly in diamond below threshold strain levels for phonon instability. We identify the pathway to metallization within six-dimensional strain space for different sample geometries. We also explore phonon-instability conditions that promote phase transition to graphite. These findings offer opportunities for tailoring properties of diamond via strain engineering for electronic, photonic, and quantum applications.

elastic strain engineering | machine learning | multiscale simulations | metallic diamond | materials under extreme conditions

The exceptionally high hardness and stiffness of diamond, along with its many extreme physical properties and biocompatibility, make it a desirable candidate material for a wide variety of mechanical, electronic, photonic, biomedical, and energy applications. Recent experimental discovery (1) has established that monocrystalline and polycrystalline diamond nanoneedles (diameter ∼300 nm) can be deformed reversibly to local elastic tensile strains higher than 9% and 3.5%, respectively, at room temperature. These findings have been independently corroborated by subsequent deformation experiments (2) on nanoscale pillars produced by focused ion beam slicing of natural diamond specimens. Here the largest local tensile strains of 13.4% and 9.6%, respectively, are realized in <100>- and <110>-oriented nanoneedles (2) of single-crystal diamond during bending, whereas the corresponding maximum local compressive strains of −14% and −10.1%, respectively, are observed on the compression side.

These advances offer hitherto unexplored possibilities whereby functional properties of diamond can be purposely tailored and significantly altered through strain engineering. One pathway to accomplish this goal is to develop ab initio calculations and experimentally validated finite element simulations for reversible straining. Results from these analyses are then used to train machine-learning algorithms to find optimized material properties for diamond for different geometries and loading conditions by scanning all possible combinations of deformation states within the general six-dimensional (6D) strain space employing reasonable computing resources (3).

Motivated by such possibilities, we focus here specifically on addressing the following scientific questions:

1) Is it possible to metallize diamond at room temperature and pressure, from its natural unstrained state with an ultrawide electronic bandgap of 5.6 eV to full metallization with 0-eV bandgap, without phonon instability or structural transformation such as graphitization, solely through the imposition of strain?
2) What are the strain states and the lowest strain energy density required to achieve such "safe" bandgap metallization among all possible combinations of straining?
3) How much of such "safe" metallization can be realized within deformation conditions that have already been shown to be achievable experimentally?
4) How do crystallographic and geometric variables influence the metallization of diamond?
5) What are the conditions that trigger indirect-to-direct bandgap electronic transition, or a competing graphitization phase change, in diamond under straining?

Here we demonstrate that it is possible to achieve 0-eV electronic bandgap in diamond exclusively through the imposition of reversible elastic strains, without triggering phonon instability or phase change (4, 5). This discovery implies that reversible metallization/demetallization is feasible through judicious design of mechanical loading conditions and geometry in nanoscale diamond. We further show that "safe" metallization can be achieved at elastic strain energy density values on the order of 95 to 275 meV/Å^3, comparable to what has been demonstrated in experiments of reversible deformation of diamond nanopillars (1, 2). Our results also reveal that even simple bending of low-index <110>-oriented monocrystalline diamond nanoneedles can effectively reduce the bandgap from 5.6 eV down to 0 eV without

Significance

Identifying the conditions for complete metallization of diamond solely through mechanical strain is an important scientific objective and technological demonstration. Through quantum mechanical calculations, continuum mechanics simulations validated by experiments, and machine learning, we show here that reversible metallization can be achieved in diamond deformed below threshold elastic strain levels for failure or phase transformation. The general method outlined here for deep elastic strain engineering is also applicable to map the strain conditions for indirect-to-direct bandgap transitions. Our method and findings enable extreme alterations of semiconductor properties via strain engineering for possible applications in power electronics, optoelectronics, and quantum sensing.

Author contributions: Z.S., M.D., A.S., J.L., and S.S. designed research; Z.S., M.D., and E.T. performed research; Z.S., M.D., E.T., A.S., J.L., and S.S. analyzed data; and Z.S., M.D., A.S., J.L., and S.S. wrote the paper.

Reviewers: J.L., IMDEA Materials Institute; and N.M., École Polytechnique Fédérale de Lausanne.

Competing interest statement: Z.S., M.D., J.L., and S.S. are coinventors on a patent application based on the invention reported in this paper.

[1]Z.S. and M.D. contributed equally to this work.

[2]To whom correspondence may be addressed. Email: SSuresh@ntu.edu.sg, liju@mit.edu, or mingdao@mit.edu.

This article contains supporting information online at https://www.pnas.org/lookup/suppl/doi:10.1073/pnas.2013565117/-/DCSupplemental.

First published October 5, 2020.

phonon instability, at about 10.8% local compressive elastic strain. Further bending the nanoneedle can, however, induce phonon instabilities (5) that lead to irreversible $sp^3 \rightarrow sp^2$ (diamond to graphite) phase transition or fracture. Indeed, plasticity induced by such $sp^3 \rightarrow sp^2$ phase transition has recently been observed in the large bending of a single-crystalline diamond pillar (6), substantially agreeing with our calculations. Similar graphitization transition is also seen in nanoindentation experiments (7). Navigating the treacherous elastic strain space above 80 meV/Å^3 or at >9% local compressive or tensile principal elastic strain to induce complete metallization in diamond without encountering phonon instabilities is a "holy grail" demonstration for power electronics, optoelectronics, and quantum sensing systems.

Whether mechanically strained or not, the absence of imaginary phonon frequency for the wavevector in the entire Brillouin zone is the hallmark of a locally stable crystal lattice (5, 8, 9). If a strained perfect crystal lattice has a stable phonon band structure, then at $T = 0$ K and in the absence of defects such as free surfaces, interfaces and dislocations, this lattice is guaranteed to avoid spontaneous phase transition or defect nucleation. Consequently, phonon stability is the minimal requirement for lattice stability and loading reversibility (5). If such a phonon-stable diamond can have zero electronic bandgap, $E_g = 0$ eV (reduced from $E_g = 5.6$ eV at zero strain), then this extreme electronic material (10) is expected to demonstrate unprecedented functional flexibility, from ultrawide bandgap semiconductor to the far-infrared and even metallic, in one material, without any change in chemical composition and possibly under dynamic loading. The electronic band structures of diamond under tensorial strain can be predicted with high accuracy based on ab initio density functional theory (DFT) followed by many-body GW (G, Green's function; W, screened Coulomb interaction) calculations (11). However, because GW calculations are computationally expensive, it is necessary to invoke a stress–strain constitutive law for modeling large elastic deformation of diamond in any arbitrary sample geometry, along with fast proxy models for the electronic and phonon band structures. In this work, we employ machine-learning algorithms of band structures (3) based on an artificial neural network (NN) approach, so as to perform coupled ab initio and finite element calculations with constitutive laws based on NNs (see *Methods* for details). The coupling of this simulation to loading and/or device geometry optimization (12) and computer-aided design (13) provides a unique and hitherto unknown pathway to engineer "safe" metallization in diamond.

We first present some 6D strain states in Fig. 1 which make the bandgap of diamond vanish without phonon instability or graphitization. In the crystallographic [100][010][001] coordinate frame, our calculations show that one such complete and "safe" metallization occurs when the local 6D strain state is (0.0536, −0.0206, −0.056, 0.0785, 0.0493, 0.0567). Fig. 1*A* is a ***k***-space plot of the GW electronic band structure for diamond deformed to this particular 6D strain state, resulting in a direct metal (see *SI Appendix*, Fig. S1 for comparison of GW electronic band structure with that for DFT). Contours of strain energy density are plotted in two-dimensional (2D) strain space in Fig. 1*B* where the star symbol in black, represents $h = 98.7$ meV/Å^3. Note that the strains and strain energy density values in Fig. 1 are comparable to the values achieved experimentally (1, 2) in reversible ultra-large elastic bending of diamond nanoneedles or pillars.

Fig. 2 further illustrates our discovery of the region of "safe" metallization of diamond without phonon instability and demonstrates reversible indirect-to-direct bandgap transitions under large elastic strains. Possible strain states in the three-dimensional (3D) space of normal strains ε_{11}, ε_{22}, and ε_{33}, spanning −20% (i.e., compressive strain of 0.2) to +10% (i.e., tensile strain of 0.1) within which "safe" metallization is induced (highlighted in brown color) are shown in Fig. 2*A*. Regions of metallization are also plotted in Fig. 2*B* in the 2D strain space of ε_{11}versus ε_{22}, with the other four strain components held fixed (i.e., formed as a result of 2D projection out of 3D strain region tessellated by cubes on to the plane $\varepsilon_{33} = -0.056$ in Fig. 2*A*). The triangle data points of different colors in Fig. 2*B* represent results of computational simulations of the effect of mechanical strain on bandgap and band structure. Two types of "safe" metallization, direct metal and indirect metal (where the band-edge transition is indirect, i.e., from two different ***k***-points), are identified. The 2D region of direct metal, shaded in brown, encompasses the strain state represented by the star symbol, which was discussed in Fig. 1. This zone is embedded within the strain space of direct bandgap (blue region, Fig. 2*B*). The region of indirect metal, also shaded in brown, is surrounded by the white zone representing the strain space for indirect bandgap (comprising magenta-colored data points from our simulation). In Fig. 2*C*, the GW band structure is plotted in the ***k***-space to illustrate such indirect-metal state at point c (Fig. 2*B*) inside this zone of "safe" metallization. Examples of nonzero direct and indirect bandgap cases indicated by the band structure plots are shown in Fig. 2 *D* and *E*, respectively. The area shaded in gray outside of the dashed lines is the region of large elastic strains and unstable metallization where phonon instability leading to

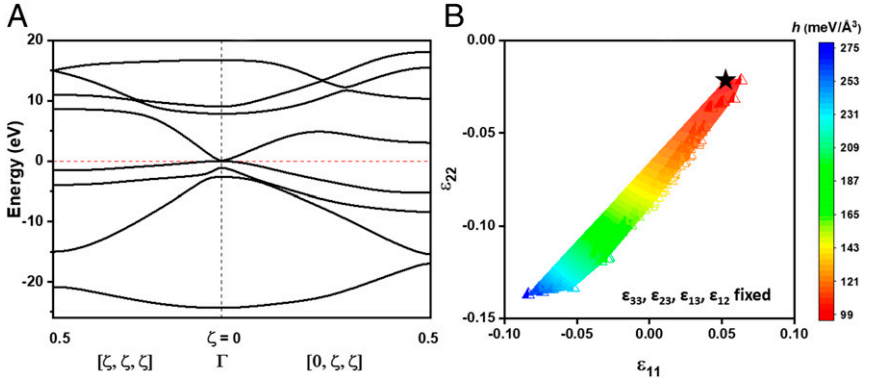

Fig. 1. Metallization of diamond. (*A*) Electronic band structure ***k***-space plot showing complete closure of bandgap leading to metallization of diamond which is subjected to deformation at a 6D strain state of (0.0536, −0.0206, −0.056, 0.0785, 0.0493, 0.0567) in the [100][010][001] coordinate frame. An entire region of strains exists for the metallization of diamond and a 2D cross-section plot of normal strain components ε_{11} and ε_{22} is illustrated in *B*. The axes in *B* are absolute strain component values of ε_{11} and ε_{22}, with the other four strain components fixed at −0.056, 0.0785, 0.0493, and 0.0567. Color contours indicate regions of constant elastic strain energy density (*h*) for different deformation states. The black star symbol denotes the strain energy density value, $h = 98.7$ meV/Å^3, which corresponds to the band structure plot shown in *A*.

defect nucleation and/or phase transition occurs (5). Fig. 2*F* reveals pronounced reduction in phonon frequency and the occurrence of soft mode associated with strain point f in Fig. 2*B* where phonon instability and associated phase transition from diamond to graphite takes place. The location of the special strain region containing metallization is not unique in a general 6D strain hyperspace and such stratified regions may exist in a broad range of semiconductors. Our findings offer a systematic strategy in the search for strain-engineered semiconductor-to-metal transition, indirect-to-direct bandgap transition, as well as phase transition.

Experiments show that diamond nanoneedles exhibit ultralarge elastic bending before fracture (1). Such deformation, resulting in local compressive strains larger than −10% and tensile strains in excess of 9%, is reversible upon release of the load. Here we apply simulations to determine bandgap modulation in bent diamond nanoneedles at maximum local strain levels that are known to be experimentally feasible (*SI Appendix*, Table S1). Fig. 3*A* schematically illustrates the method whereby a diamond indenter tip pushes on a diamond nanoneedle to induce large deformation (1). The finite element method (FEM) is used to simulate the sideward bending moment of the diamond needle upon contact with the indenter tip and account for nonlinear elasticity, orientation of the cubic lattice with respect to the needle axis, the bending direction, and possible friction between the indenter tip and the needle.

Fig. 3*B* shows FEM results of local compressive and tensile strains of the deformed geometry of <110> diamond nanoneedle, with the maximum compressive and tensile strains of −10.8% and 9.6%, respectively. The accuracy of FEM predictions is validated by direct comparison with experimentally measured indentation load plotted against displacement (1). The corresponding predictions, from our simulations, of the distribution of bandgap are also plotted in Fig. 3*B*. The onset of "safe" metallization appears in the severely strained compressive side of the nanoneedle at a local strain of −10.8%, as shown in Fig. 3*C*. The propensity toward increasingly more metal-like behavior with increasing strain is independent of friction between the indenter and the nanoneedle (see *SI Appendix*, Fig. S3). The <110> nanoneedle can withstand up to 12.1% local tensile strain before incurring phonon instability on the tensile side, at a bandgap of 0.62 eV, as shown in Fig. 3*D*. The maximum attainable local tensile strain of 9.6% on the tensile side of <110> single-crystal natural diamond samples (2), as compared to theoretical predictions of higher values (*SI Appendix*, Fig. S4 and Table S1), could be attributed to the presence of dislocations and/or other surface-related defects (14–17). The compressive side is more tolerant to deformation. The maximum attainable compressive strain could be on the order of −20% along a low-index orientation (18), suggesting that there is room for additional elastic deformation after achieving "safe" metallization in compression-dominated regions. Note that due to the zero-point motion effect (19) and the Varshni effect (20), for physical experiments performed at room temperature, the bandgap of diamond is expected to be even smaller than estimated here by 0.4 to 0.6 eV (21, 22). This understanding leads to the inference that safe metallization in diamond can occur at elastic strain levels somewhat smaller than indicated by our analysis, making it even more easily achievable than appears from the quantitative results plotted here (see *Methods* for details).

Crystallographic orientation of the nanoneedle axis is another variable determining the extent of large deformation and the resultant bandgap modulation. This orientation effect is illustrated in *SI Appendix*, Fig. S5 *A* and *B*. Among the three types of nanoneedles studied, the <110>- and <111>-oriented nanoneedles require relatively smaller tensile strains to reduce bandgap through straining, whereas the <100> orientation is the hardest orientation to reduce bandgap below 2 eV or approach metallization. This distinction can be attributed to the difference in flexibility to access all six components of the strain tensor expressed in the [100][010][001] coordinate frame. Despite the possibility of extremely large strain in a <100>-oriented nanoneedle, this orientation primarily facilitates normal strains (with the shear components ε_{23}, ε_{13}, and ε_{12} being relatively much smaller) and the resultant maximum bandgap reduction is limited before phonon instability is reached, causing fracture or phase transformation (5). For deformation of the <110>- and <111>-oriented needles, on the other hand, it is relatively easier to initiate both normal and shear strain components necessary for band structure engineering (3, 23–25) and the resultant bandgap modulation. In the <111>-oriented needles, these strain conditions further facilitate indirect-to-direct bandgap transitions in diamond. The spatial evolution of the "safe" direct bandgap regions in our nanoneedles can be found in *SI Appendix*, Fig. S5*C*. Bending direction is another geometrical factor, as shown in *SI Appendix*, Fig. S5*D*. For a low-index-oriented needle, we find bending direction has little influence on the maximum bandgap reduction in the bent needle.

Beyond the configurations considered here, more complex 3D loading geometries with holes and notches through topology optimization (26) and micro- and nanomachining of geometric features (27, 28) can be designed without exposing the metallized zone to near-surface regions (29), further increasing possibilities for metallizing diamond. These methods for deep elastic strain engineering are equally applicable to map the indirect-to-direct bandgap transition locations in diamond for the most general 6D straining case, as indicated in Fig. 2 *A*, *B*, and *D*. When strained diamond is transformed into a direct bandgap semiconductor, even only locally at the site of maximum strain, it would exhibit a fundamental enhancement in its optical transitions around the adsorption edge compared to an undeformed diamond in its natural state. This transition arises from the absence of phonon involvement (momentum change of electron) in the adsorption or emission process. Since absorbance increases exponentially with thickness in a material, a light energy conversion device based on direct bandgap semiconductor with a high adsorption coefficient and rationally engineered bandgap value would require much less thickness to absorb the same amount of light with a variety of wavelengths, from the visible to the far-infrared. These considerations could pave the way for designing high-efficiency photo detectors and emitters from ultraviolet to the far-infrared on a single piece of diamond. As photons and excitons are the primary tools for quantum information processing, this extreme ability to mold diamond's band structure will also be highly consequential for quantum sensing and quantum computing applications.

To perform simultaneous mechanical deformation and electronic properties evaluation, further studies could combine in situ nanoelectromechanical loading experiments inside a transmission electron microscope with built-in electron energy loss spectroscopy (EELS). It is known (30–32) that EELS is reliable for assessing the bandgap value (including surface plasmon mapping) as well as indirect-to-direct bandgap transition in diamond. Indentation and anviling (compression under extreme pressures) coupled with in situ photoluminescence (33–35) or cathodoluminescence (36) spectroscopy as well as electrical resistivity measurement (37) further add to the toolbox for characterization of mechanically induced properties including superconductivity of diamond (38–40).

Methods

First-Principles Calculations. The Vienna Ab initio Simulation Package (VASP) (41) was used for DFT calculations to predict the evolution of bandgap and band structure of diamond subjected to mechanical deformation. We invoked the generalized gradient approximation in the form of Perdew–Burke–Ernzerhof's (PBE) exchange-correlation (42) functional and the projector augmented wave method (43) in our DFT computation. A plane-wave basis set with an energy cutoff of 600 eV was adopted to expand the electronic wavefunctions. The Brillouin zone integration was conducted on a 13 × 13 × 13 Monkhorst–Pack (44) ***k***-point mesh. Atomic coordinates in all of the structures were relaxed until the maximum residual force was below 0.0005 meV/Å.

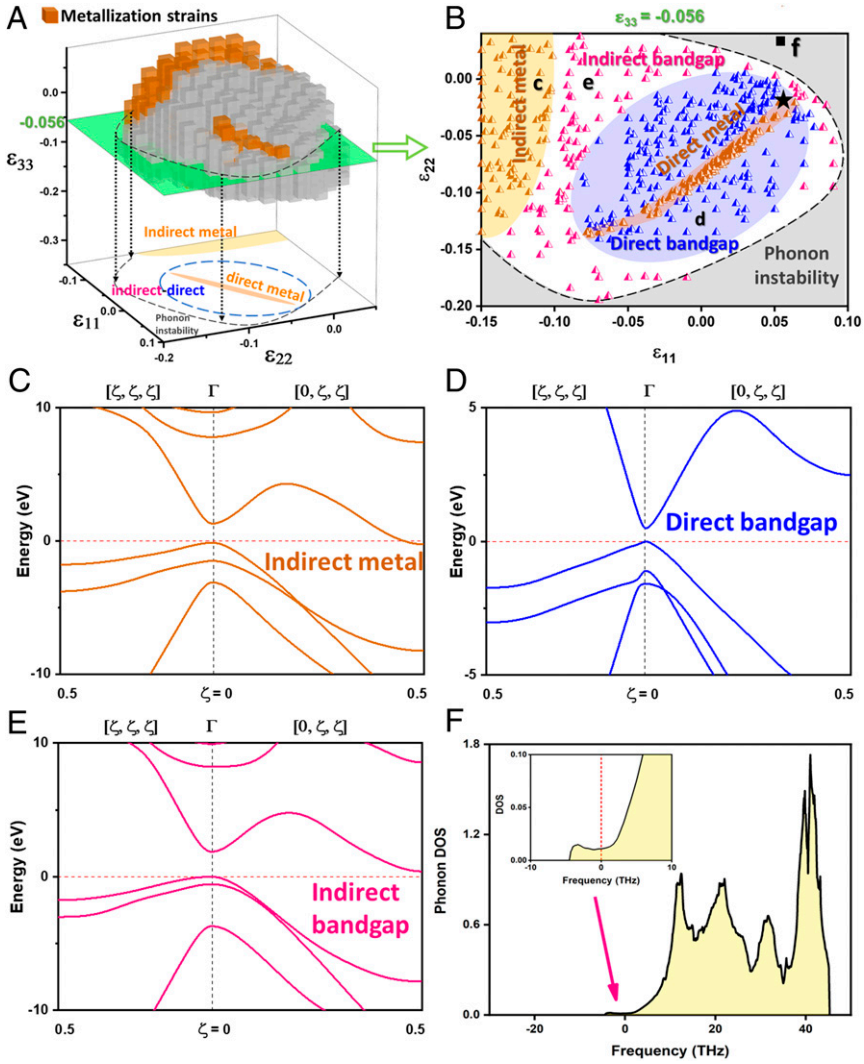

Fig. 2. Stratification of the strain hyperspace into regions of metallization and bandgap transition in diamond. (*A*) Metallization in elastically strained diamond for different values of normal strain components ε_{11}, ε_{22}, and ε_{33}, with the other three strain components held fixed. The plane with $\varepsilon_{33} = -0.056$ (colored as light green) cuts the 3D volume and results in a projection onto the ε_{11}–ε_{22} 2D plane. (*B*) Detailed characterization of the ε_{11}–ε_{22} strain space includes a region of direct metal (brown) strains within the region of direct bandgap (blue) strains and a region of indirect metal (brown) strains within the nonzero indirect bandgap strains (white zone with magenta symbols). The black star in indicates the same strain case (0.0536, −0.0206, −0.056, 0.0785, 0.0493, 0.0567) discussed in Fig. 1. An alternative visualization of the metallization strains in A is presented in *SI Appendix*, Fig. S2. (*C*) GW band structure of the diamond strained within the "safe" metallization region resulting in an indirect metal. Strained diamond (*D*) with a direct bandgap (point d in *B*) and (*E*) with an indirect bandgap (point e in *B*). The strain region of phase transformation in diamond (usually associated with phonon instability) is shaded in gray in *B*. (*F*) A phonon density of states (DOS) plot corresponding to point f in *B* illustrates imaginary phonon frequencies (indicated by the magenta arrow) when structural instability occurs. (*Inset*) A magnified view near zero frequency.

Many-body GW corrections were performed when bandgap evaluations were needed. It is known that an extremely accurate GW calculation would involve choosing "infinitely" large values for several interdependent parameters (45, 46). Given the situation that we need to construct a huge dataset of GW bandgaps for machine-learning purposes and conduct many calculations for varied 6D strain cases, we hereby struck a balance between efficiency and effectiveness. Specifically, we chose the $\boldsymbol{q}$-grid to be $6 \times 6 \times 6$, the screened cutoff to be 600 eV, and the number of bands for both dielectric matrix calculation and Coulomb hole summation to be 600. In addition, beyond the single-shot G_0W_0 method, we allowed two to three iterations of the Green's function in our calculations to obtain accurate quasi-particle shifts. This partially self-consistent GW_0 calculation is known to yield results that are in agreement with available experimental measurement for semiconductor materials (47) and better than plain DFT calculations using hybrid functionals (48). For undeformed diamond, our calculation indicates a +1.5-eV GW correction to the DFT–PBE bandgap, which matches values reported in recent literature (49). For general 6D strain cases, this correction may vary (see *SI Appendix*, Fig. S1 for an example). Diamond primitive cells were used for DFT and GW calculations. All band structures were plotted by VASP with a Wannier90 interface (50–52).

We also acknowledge that, even at 0 K, due to the quantum zero-point motion, further corrections need to be made to the electronic levels of diamond. This renormalization of bandgap could be −0.6 eV to −0.4 eV for undeformed diamond (21, 22). We consider this correction value to be negative in other cases of our interest. According to the temperature-dependent "adiabatic Allen–Heine formula" (19, 53), by setting $T = 0$ to zero-out the Bose–Einstein occupancy factors, the zero-point renormalization of the band structure ($\Delta E_{n\boldsymbol{k}}^{\mathrm{ZP}}$) arising from the electron-phonon interaction could be expressed as

$$\Delta E_{n\boldsymbol{k}}^{\mathrm{ZP}} \equiv \Delta E_{n\boldsymbol{k}}(T=0) = \sum_{\nu} \int_{\Omega_{\mathrm{BZ}}} d\boldsymbol{q} \left[\sum_{n'} \frac{\left| g_{nn'\nu}(\boldsymbol{k},\boldsymbol{q}) \right|^2}{\varepsilon_{n\boldsymbol{k}} - \varepsilon_{n'\boldsymbol{k}+\boldsymbol{q}}} \right] + \Sigma_{n\boldsymbol{k}}^{\mathrm{DW}},$$

where $\varepsilon_{n\boldsymbol{k}}$ is the single-particle eigenvalue of an electron with crystal momentum $\boldsymbol{k}$ in the band n, the integral is over the Brillouin zone of volume

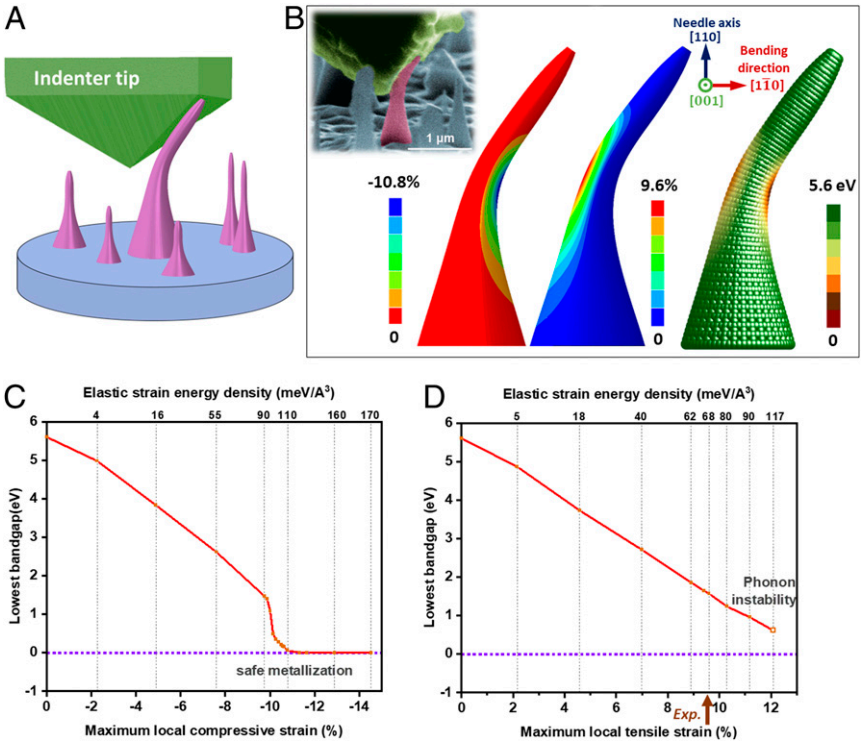

Fig. 3. Metallization in diamond nanoneedles. (*A*) Schematic of the bending of single-crystalline diamond nanoneedle by diamond nanoindenter tip inside a scanning electron microscope. (*B*) FEM predictions of the local compressive and tensile strain distributions (left and middle needle, respectively) and predictions by the machine-learning algorithm of the distribution of bandgap (right needle) for a diamond nanoneedle with its <110> crystallographic direction aligned with the needle axis. (*Inset*) A scanning electron micrograph of the deformed nanoneedle during the bending experiment, from ref. 1. Reprinted with permission from AAAS. (*C*) Increasing magnitude of bending in the <110> nanoneedle causes a significant reduction in bandgap of diamond from 5.6 eV (zero strain) down to 0 eV for a maximum local compressive strain of −10.8% (the corresponding maximum local tensile strain on the tension side is 9.6%). (*D*) Local tensile strain beyond 12.1% results in fracture or graphitization on the tensile side of the nanoneedle according to our ab initio calculations, even when there are no preexisting defects. See also Movie S1 for the evolution of elastic strain energy, bandgap, and the corresponding band structure at the maximum compression site in the nanoneedle, showing the medialization process.

Ω_{BZ}, the outermost summation is over all phonon branches ν, and the first-order electron–phonon matrix elements $g_{nn'\nu}(\boldsymbol{k},\boldsymbol{q})$ describe the scattering from an initial state with wave vector $\boldsymbol{k}$ to a final state with wave vector $\boldsymbol{k}+\boldsymbol{q}$, with the emission or absorption of a phonon with crystal momentum $\boldsymbol{q}$ belonging to the phonon branch ν. The first term on the right-hand side is the Fan–Migdal self-energy term (54) and the Σ^{DW}_{nk} term is the Debye–Waller (DW) self-energy term. Given the DW term are normally much smaller than the Fan-Migdal term [about 1:5 in diamond (21)], the deciding factors to the sign of ΔE^{ZP}_{nk} are the denominators $\varepsilon_{nk}-\varepsilon_{n'k+q}$. The change of bandgap can be qualitatively evaluated by considering the relative shift of the valence band maximum (VBM) and conduction band minimum (CBM). For VBM, we can further assume the coupling primarily comes from scattering within the valence bands. Since no values of $\varepsilon_{n'k+q}$ in the valence bands can be larger than $\varepsilon_{n_{VBM}k}$, the denominators $\varepsilon_{n_{VBM}k}-\varepsilon_{n'k+q}$ would always be positive and the resultant $\Delta E^{ZP}_{n_{VBM}k}$ would also be positive. Similarly, $\varepsilon_{n_{CBM}k}-\varepsilon_{n'k+q}$ at CBM and the resultant $\Delta E^{ZP}_{n_{CBM}k}$ would always be negative. The upward shift of VBM and downward shift of CBM would, therefore, result in an overall reduction in the computed bandgap of diamond. Therefore, from this perspective, we provided a generally conservative estimation of the strain magnitude required for engineering the bandgap. The actual bandgap may be even smaller than we predicted at particular strain levels as in Fig. 3, allowing metallization to be safely achieved more easily.

To identify the phonon instability boundaries, we performed phonon stability calculations for densely sampled strain points in 3D or 2D strain space. These calculations were primarily carried out using the VASP-Phonopy package (55); 3 × 3 × 3 supercells were created, and phonon calculations were conducted with a 3 × 3 × 3 ***k***-point mesh. Whenever accurate phonon stability check was needed for diamond primitive cell, density functional perturbation theory (56) as implemented in Quantum ESPRESSO (57) was adopted, with a dense 11 × 11 × 11 ***k***-grid and 6 × 6 × 6 ***q***-grid.

Machine Learning. The bandgap distribution in diamond nanoneedles deformed to different strains was computed using machine-learning algorithms. This is done by representing deformation as a strain tensor and using an artificial NN to fit the strain states against respective bandgap values obtained accurately by first-principles calculations. The NN fitting is implemented within the TensorFlow framework, an end-to-end open-source machine-learning platform released by Google (58). The specific design, similar to our previous work (3), involves a feed-forward architecture with hidden layers capable of learning the variations of band structure and bandgap with respect to large mechanical deformation. In order to integrate both the PBE and GW datasets we prepared by first-principles calculations and to produce more consistent and accurate machine learning outcomes, the same "data fusion" technique as in our work in ref. 3 was used. It took the quantitative advantage of PBE and the qualitative advantage of GW by interpolating between them to achieve decent NN fitting results with only ~10^4 PBE and ~10^3 GW calculations, successfully alleviating the need for the otherwise impractical submillion-level amount of computations.

Finite Element Modeling. The ABAQUS (Dassault Systèmes Simulia Corp.) software package was employed to conduct FEM analyses on specimen models, which replicated the 3D geometry of the diamond nanoneedles. Both the cube corner indenter and the nanoneedle were specified as deformable solids using the same elastic properties. A frictional sliding contact was specified between the nanoneedle surface and the indenter surface. Geometric nonlinearity induced by large deformation was accounted for. Neo-Hookean nonlinear elasticity model was used to simulate large deformation. The equivalent small-strain Young's modulus was given as 1,100 GPa and the Poisson's ratio 0.0725 (1). Since friction makes a negligible change to the deformed shape, the friction coefficient between the nanoneedle and the indenter was taken to be 0.1.

Data Availability. Data supporting the findings of this study are available in the paper and *SI Appendix*.

ACKNOWLEDGMENTS. We acknowledge support from the Office of Naval Research Multidisciplinary University Research Initiative grant N00014-18-1-2497. Z.S. and E.T. acknowledge support by the Massachusetts Institute of Technology (MIT) Skoltech Next Generation Program 2016-7/NGP. E.T. and A.S. acknowledge support by the Center for Integrated Nanotechnologies, an Office of Science User Facility operated for the US Department of Energy Office of Science by Los Alamos National Laboratory (Contract 89233218CNA000001) and Sandia National Laboratories (Contract DE-NA-0003525). M.D. acknowledges support from MIT J-Clinic for Machine Learning and Health. S.S. acknowledges support from Nanyang Technological University through the Distinguished University Professorship. We thank Dr. Hua Wang from MIT for conducting independent computational checks and verifications.

1. A. Banerjee *et al*., Ultralarge elastic deformation of nanoscale diamond. *Science* **360**, 300–302 (2018).
2. A. Nie *et al*., Approaching diamond's theoretical elasticity and strength limits. *Nat. Commun.* **10**, 5533 (2019).
3. Z. Shi *et al*., Deep elastic strain engineering of bandgap through machine learning. *Proc. Natl. Acad. Sci. U.S.A.* **116**, 4117–4122 (2019).
4. O. H. Nielsen, Optical phonons and elasticity of diamond at megabar stresses. *Phys. Rev. B Condens. Matter* **34**, 5808–5819 (1986).
5. X. Liu, J. Gu, Y. Shen, J. Li, Crystal metamorphosis at stress extremes: How soft phonons turn into lattice defects. *NPG Asia Mater.* **8**, e320 (2016).
6. B. Regan *et al*., Plastic deformation of single-crystal diamond nanopillars. *Adv. Mater.* **32**, 1906458.
7. Y. G. Gogotsi, A. Kailer, K. G. Nickel, Transformation of diamond to graphite. *Nature* **401**, 663–664 (1999).
8. X. Liu, J. Gu, Y. Shen, J. Li, C. Chen, Lattice dynamical finite-element method. *Acta Mater.* **58**, 510–523 (2010).
9. J. Li, K. J. Van Vliet, T. Zhu, S. Yip, S. Suresh, Atomistic mechanisms governing elastic limit and incipient plasticity in crystals. *Nature* **418**, 307–310 (2002).
10. J. Y. Tsao *et al*., Ultrawide-bandgap semiconductors: Research opportunities and challenges. *Adv. Electron. Mater.* **4**, 1600501 (2018).
11. F. Aryasetiawan, O. Gunnarsson, The GW method. *Rep. Prog. Phys.* **61**, 237–312 (1998).
12. O. Sigmund, K. Maute, Topology optimization approaches. *Struct. Multidiscipl. Optim.* **48**, 1031–1055 (2013).
13. S. Krish, A practical generative design method. *Comput. Aided Des.* **43**, 88–100 (2011).
14. X. Li, Y. Wei, L. Lu, K. Lu, H. Gao, Dislocation nucleation governed softening and maximum strength in nano-twinned metals. *Nature* **464**, 877–880 (2010).
15. J. Xiao *et al*., Dislocation behaviors in nanotwinned diamond. *Sci. Adv.* **4**, eaat8195 (2018).
16. J. R. Greer, W. D. Nix, Nanoscale gold pillars strengthened through dislocation starvation. *Phys. Rev. B* **73**, 245410 (2006).
17. C. Chisholm *et al*., Dislocation starvation and exhaustion hardening in Mo alloy nanofibers. *Acta Mater.* **60**, 2258–2264 (2012).
18. A. Nie *et al*., Direct observation of room-temperature dislocation plasticity in diamond. *Matter* **2**, 1222–1232 (2020).
19. P. B. Allen, V. Heine, Theory of the temperature dependence of electronic band structures. *J. Phys. C Solid State Phys.* **9**, 2305–2312 (1976).
20. Y. P. Varshni, Temperature dependence of the energy gap in semiconductors. *Physica* **34**, 149–154 (1967).
21. F. Giustino, S. G. Louie, M. L. Cohen, Electron-phonon renormalization of the direct band gap of diamond. *Phys. Rev. Lett.* **105**, 265501 (2010).
22. S. Poncé *et al*., Verification of first-principles codes: Comparison of total energies, phonon frequencies, electron–phonon coupling and zero-point motion correction to the gap between ABINIT and QE/Yambo. *Comput. Mater. Sci.* **83**, 341–348 (2014).
23. G. L. Bir, G. E. Pikus, *Symmetry and Strain-Induced Effects in Semiconductors*, (Wiley, 1974).
24. I. Yu. Sahalianov, T. M. Radchenko, V. A. Tatarenko, G. Cuniberti, Y. I. Prylutskyy, Straintronics in graphene: Extra large electronic band gap induced by tensile and shear strains. *J. Appl. Phys.* **126**, 054302 (2019).
25. J. C. Hensel, H. Hasegawa, M. Nakayama, Cyclotron resonance in uniaxially stressed silicon. II. Nature of the covalent bond. *Phys. Rev.* **138**, A225–A238 (1965).
26. N. Aage, E. Andreassen, B. S. Lazarov, O. Sigmund, Giga-voxel computational morphogenesis for structural design. *Nature* **550**, 84–86 (2017).
27. D.-D. Cui, L.-C. Zhang, Nano-machining of materials: Understanding the process through molecular dynamics simulation. *Adv. Manuf.* **5**, 20–34 (2017).
28. G. M. Robinson, M. J. Jackson, A review of micro and nanomachining from a materials perspective. *J. Mater. Process. Technol.* **167**, 316–337 (2005).
29. P. Hess, Predictive modeling of intrinsic strengths for several groups of chemically related monolayers by a reference model. *Phys. Chem. Chem. Phys.* **20**, 7604–7611 (2018).
30. S. Korneychuk, G. Guzzinati, J. Verbeeck, Measurement of the indirect band gap of diamond with EELS in STEM. *phys. Status Solidi (a)* **215**, 1800318 (2018).
31. C. S. Granerød, W. Zhan, Ø. Prytz, Automated approaches for band gap mapping in STEM-EELS. *Ultramicroscopy* **184**, 39–45 (2018).
32. Ph. Redlich, F. Banhart, Y. Lyutovich, P. M. Ajayan, EELS study of the irradiation-induced compression of carbon onions and their transformation to diamond. *Carbon* **36**, 561–563 (1998).
33. B. Li *et al*., Diamond anvil cell behavior up to 4 Mbar. *Proc. Natl. Acad. Sci. U.S.A.* **115**, 1713–1717 (2018).
34. L. Dubrovinsky, N. Dubrovinskaia, V. B. Prakapenka, A. M. Abakumov, Implementation of micro-ball nanodiamond anvils for high-pressure studies above 6 Mbar. *Nat. Commun.* **3**, 1163 (2012).
35. T. Yin *et al*., High-pressure-induced comminution and recrystallization of CH3NH3PbBr3 nanocrystals as large thin nanoplates. *Adv. Mater.* **30**, 1705017 (2018).
36. X. Fu *et al*., Tailoring exciton dynamics by elastic strain-gradient in semiconductors. *Adv. Mater.* **26**, 2572–2579 (2014).
37. L. Lu, Y. Shen, X. Chen, L. Qian, K. Lu, Ultrahigh strength and high electrical conductivity in copper. *Science* **304**, 422–426 (2004).
38. E. A. Ekimov *et al*., Superconductivity in diamond. *Nature* **428**, 542–545 (2004).
39. E. A. Ekimov *et al*., Structure and superconductivity of isotope-enriched boron-doped diamond. *Sci. Technol. Adv. Mater.* **9**, 044210 (2009).
40. C. Liu, X. Song, Q. Li, Y. Ma, C. Chen, Superconductivity in compression-shear deformed diamond. *Phys. Rev. Lett.* **124**, 147001 (2020).
41. G. Kresse, J. Furthmüller, Efficiency of ab-initio total energy calculations for metals and semiconductors using a plane-wave basis set. *Comput. Mater. Sci.* **6**, 15–50 (1996).
42. J. P. Perdew, K. Burke, M. Ernzerhof, Generalized gradient approximation made simple. *Phys. Rev. Lett.* **77**, 3865–3868 (1996).
43. P. E. Blöchl, Projector augmented-wave method. *Phys. Rev. B Condens. Matter* **50**, 17953–17979 (1994).
44. H. J. Monkhorst, J. D. Pack, Special points for Brillouin-zone integrations. *Phys. Rev. B* **13**, 5188–5192 (1976).
45. B. D. Malone, M. L. Cohen, Quasiparticle semiconductor band structures including spin-orbit interactions. *J. Phys. Condens. Matter* **25**, 105503 (2013).
46. B.-C. Shih, Y. Xue, P. Zhang, M. L. Cohen, S. G. Louie, Quasiparticle band gap of ZnO: High accuracy from the conventional G^0W^0 approach. *Phys. Rev. Lett.* **105**, 146401 (2010).
47. M. S. Hybertsen, S. G. Louie, Electron correlation in semiconductors and insulators: Band gaps and quasiparticle energies. *Phys. Rev. B Condens. Matter* **34**, 5390–5413 (1986).
48. J. Kaczkowski, Electronic structure of some wurtzite semiconductors: Hybrid functionals vs. Ab initio many body calculations. *Acta Phys. Pol. A* **121**, 1142–1144 (2012).
49. K. Ramakrishna, J. Vorberger, Ab initio dielectric response function of diamond and other relevant high pressure phases of carbon. *J. Phys. Condens. Matter* **32**, 095401 (2020).
50. A. A. Mostofi *et al*., An updated version of wannier90: A tool for obtaining maximally-localised wannier functions. *Comput. Phys. Commun.* **185**, 2309–2310 (2014).
51. I. Souza, N. Marzari, D. Vanderbilt, Maximally localized Wannier functions for entangled energy bands. *Phys. Rev. B* **65**, 035109 (2001).
52. N. Marzari, D. Vanderbilt, Maximally localized generalized Wannier functions for composite energy bands. *Phys. Rev. B* **56**, 12847–12865 (1997).
53. F. Giustino, Electron-phonon interactions from first principles. *Rev. Mod. Phys.* **89**, 015003 (2017).
54. H. Y. Fan, Temperature dependence of the energy gap in semiconductors. *Phys. Rev.* **82**, 900–905 (1951).
55. A. Togo, I. Tanaka, First principles phonon calculations in materials science. *Scr. Mater.* **108**, 1–5 (2015).
56. X. Gonze, Perturbation expansion of variational principles at arbitrary order. *Phys. Rev. A* **52**, 1086–1095 (1995).
57. P. Giannozzi *et al*., QUANTUM ESPRESSO: A modular and open-source software project for quantum simulations of materials. *J. Phys. Condens. Matter* **21**, 395502 (2009).
58. M. Abadi *et al*., "TensorFlow: A system for large-scale machine learning" in *Proceedings of the 12th USENIX Conference on Operating Systems Design and Implementation, OSDI'16*, (USENIX Association, 2016), pp. 265–283.